Chapter 2

Simplified Analytical Analysis of Radial Flux Permanent Magnet Machine with Saturated Teeth

2.1 Introduction

Since the inception, the open slot machines have been popular among the researcher due to the ease of the stator manufacturing. Subsequently, numerous analytical analysis methods for open slot PM machine have been developed [87]- [130]. Moreover, in certain cases, the semicolsed slot of the machine is approximated and analysed as open slot machine [93]- [94], [117]. These analyses are either based on the conformal mapping or subdomain analytical methods. Moreover, the authors assumed stator and rotor cores are infinitely permeable. Recently, using frozen permeability method, the papers [141], [143]- [144] have illustrated the influence of the magnetic saturation and electric loading on the machine performance. These researches comprehensively describe the effect of change in magnetic properties of the stator due the magnetic saturation, on the cogging torque, back EMF and winding inductance. Basically, these parameters are analysed at no-load, and used for the prediction of on-load machine performance such as average torque, on-load voltage and torque ripple. Hence, the influence of magnetic saturation on the machine performance is not accounted by previously developed analytical model. Therefore, researchers focused on the analytical analysis for the saturated PM machines [137]- [140]. These analysis are computationally complex as solution contains combination of two solutions of governing field equation. (solution 1: periodic function in radial direction and solution2: periodic function in peripheral direction). Hence, in the present chapter, a simplified analytical model is developed for the radial flux PM machine with saturated teeth.

2.2 Analysis of Saturated PM Machine

Table 2.1: Dimensional Details of Saturated PM Machine

Machine's Parameters	Values
No of pole Pairs (P)	2
No of Slots (Q)	6
Magnet Inner Radius R_1	25 mm
Magnet Outer Radius R_2	29 mm
Stator Bore Radius R_3	30 mm
Slot Outer Radius R_4	40 mm
Stator Outer Radius R_5	50 mm
Slot Angle α	$\frac{\pi}{Q}$
Teeth Angle β	$\frac{\pi}{Q}$
Magnet Pitch θ_m	π/P
B_r, μ_r	1.1T,1.05
Teeth Relative Permeability μ_j	variable

Prior to the development of an analytical model for saturated PM machine, a FEM simulation of the model is carried out. The dimensional details of the machine used for simulation in FEM are given in the table 2.1. Rotor core is assumed to be infinitely permeable and simulated with $\mu_r = 4000$, and stator is assigned with the steel 1010 material, whose BH characteristic is depicted in the Figure-2.1. The machine is analysed on the loading condition as a sinusoidal drive with current density of $5A/mm^2$ to analyse the magnetic saturation in stator. Though the local saturation in the stator core depends on the the electrical loading and load angle, but the variation in the local saturation is noticed as periodic and less fluctuating. Hence, at an arbitrary time, say $time = 0.001sec$, the magnetic relative permeability of the stator is depicted in the Figure-2.2. The initial FEM investigation shows the relative permeability of the core is more than 50 during magnetic saturation. In view of this, the analytical model is developed for analysis of the saturated PM machine in following section.

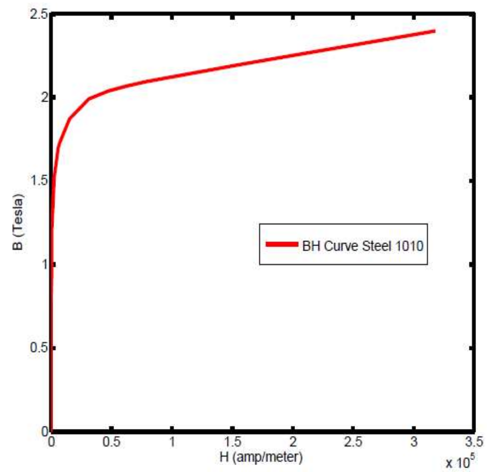

Figure 2.1: BH Characteristics of the Stator Steel

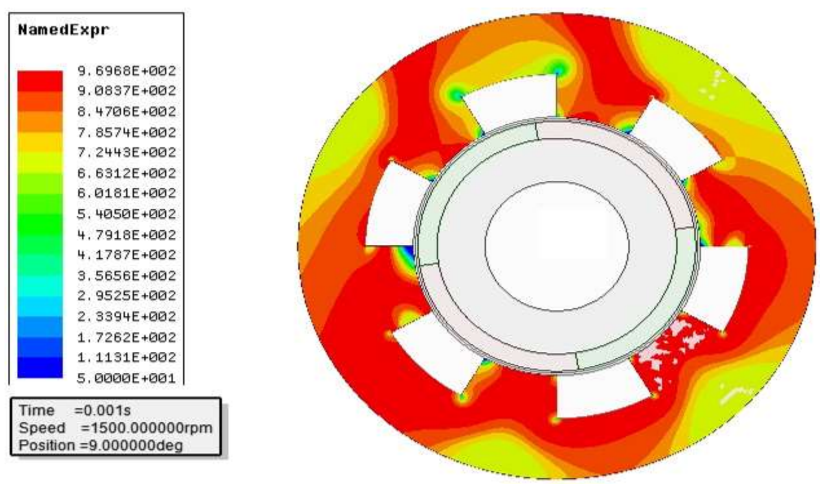

Figure 2.2: Relative Permeability of Stator Core at t=0.001 sec

2.3 Analytical Analysis of the Machine

For obtaining the field solution, the saturated PM machine can be divided into (4+2Q) subdomain regions, where Q represents number of slots. However, in the practical applications, the electrical loading influences magnetic saturation level of the teeth. Hence, the complexity of the problem is reduced due to reduction in subdomain regions from (4+2Q) to (2+2Q) as shown in the Figure-2.3.

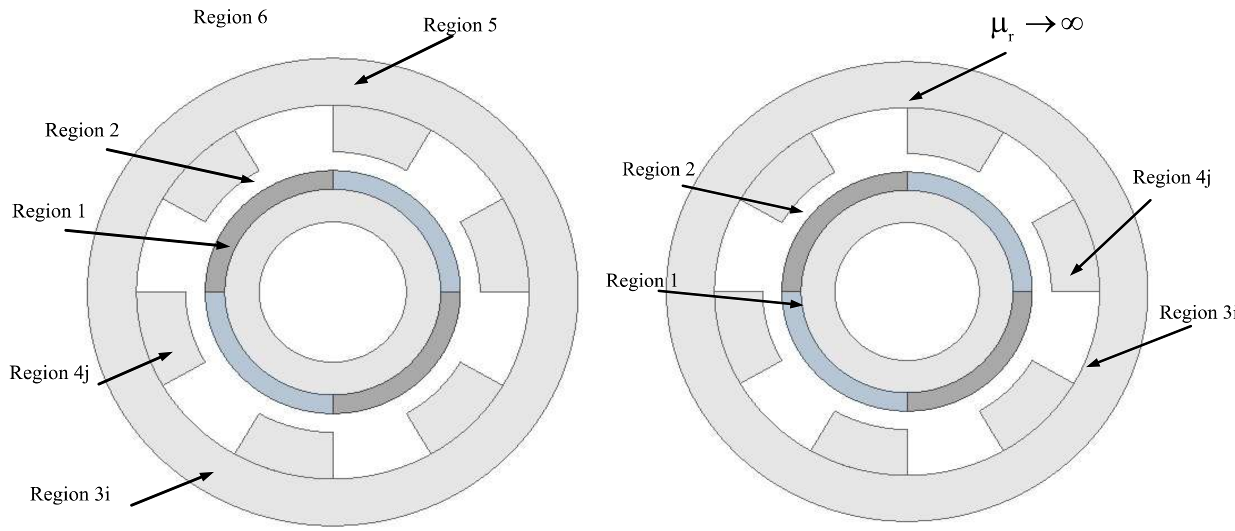

(a) (4+2Q) Subdomain (b) (2+2Q) Subdomain

Figure 2.3: Subdomain Details of Saturated PM Machine

2.3.1 No Load Vector Potential Prediction in Machine

The simplified machine model is divided into (2+2Q) subdomain viz., region 1 (permanent magnet region), region 2 (airgap region), region 3i (slots region), and region 4j (teeth regions) as shown in the Figure-2.4. The relative permeability of the individual teeth is different and changes with time/position. The analysis is carried out for arbitrary relative permeability of the teeth and hence, it is capable of accounting the teeth saturation level using FEM analysis. The assumptions used for obtaining the no load magnetic field distribution in the machine are summarized as follow:

1. Stator yoke is assumed to be infinite permeable. However, the magnetic saturation of yoke can be accounted by use of two additional Laplacian regions having finite permeability for both stator yoke and outer region.

2. Permeability of teeth is finite and arbitrary. However, the individual teeth permeability changes with time or rotor position in a saturated machine. This can be accounted by use of nonlinear FEM modeling of PM machine. Furthermore, the permeability of teeth is assumed to be real as the analytical modeling is not accounting for hysteresis loss in the teeth.

3. The rotor back iron is assumed to be infinitely permeable.

4. The flux falling on the lateral edge of the teeth normally. This is valid assumption, as the relative permeability of teeth during saturation is more than 50, and in this case the flux lines fall approximately normal [79].

5. The demagnetization characteristic curve of PMs is linear.

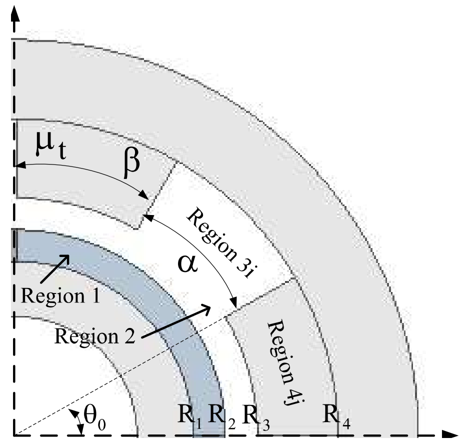

Figure 2.4: Subdomain Description of the Machine

According to the geometrical description of machine, shown in the Figure-2.4, R_1, R_2, R_3, and R_4 represent the outer radius of the rotor yoke, the outer radius of permanent magnet, the inner radius of stator bore or slot, and the radius of the slot bottom, respectively. The PM region, airgap region, slots region and teeth regions are bounded by (Region 1(PM Region): $r \in [R_1, R_2]$ & $\theta \in [0, 2\pi]$), (Region 2(Airgap Region): $r \in [R_2, R_3]$ & $\theta \in [0, 2\pi]$), (Region 3i(Slots Region): $r \in [R_3, R_4]$) & $\theta \in [\theta_o, \theta_o + \alpha]$, and (Region 4j(Teeth Region): $r \in [R_3, R_4]$ & $\theta \in [\theta_o + \alpha, \theta_o + \alpha + \beta]$), repectively.

The magnetic vector potential $\mathbf{A_z}(r, \theta)$, which is defined as $\mathbf{B} = \nabla \times \mathbf{A}$ is used for the formulation of the governing field equations in all subdomain. With Coulomb gauge $\nabla.\mathbf{A} = 0$, the governing equations are,

Region 1(PM Region): $r \in [R_1, R_2]$ & $\theta \in [0, 2\pi]$;

$$\frac{\partial^2 \mathbf{A_1}}{\partial r^2} + \frac{\partial \mathbf{A_1}}{r \partial r} + \frac{1}{r^2} \frac{\partial^2 \mathbf{A_1}}{\partial \theta^2} = \frac{\mu_o}{r} \frac{\partial \mathbf{M_r}}{\partial \theta} \tag{2.1}$$

Region 2(Airgap Region): $r \in [R_2, R_3]$ & $\theta \in [0, 2\pi]$;

$$\frac{\partial^2 \mathbf{A_2}}{\partial r^2} + \frac{\partial \mathbf{A_2}}{r \partial r} + \frac{1}{r^2} \frac{\partial^2 \mathbf{A_2}}{\partial \theta^2} = 0 \tag{2.2}$$

Region 3i(Slots Region): $r \in [R_3, R_4]$ & $\theta \in [\theta_o, \theta_o + \alpha]$;

$$\frac{\partial^2 \mathbf{A_{3i}}}{\partial r^2} + \frac{\partial \mathbf{A_{3i}}}{r \partial r} + \frac{1}{r^2} \frac{\partial^2 \mathbf{A_{3i}}}{\partial \theta^2} = 0 \tag{2.3}$$

and finally,

Region 4j(Teeth Region): $r \in [R_3, R_4]$ & $\theta \in [\theta_o + \alpha, \theta_o + \alpha + \beta]$;

$$\frac{\partial^2 \mathbf{A_{4j}}}{\partial r^2} + \frac{\partial \mathbf{A_{4j}}}{r \partial r} + \frac{1}{r^2}\frac{\partial^2 \mathbf{A_{4j}}}{\partial \theta^2} = 0 \tag{2.4}$$

where, θ_o is initial position of stator first slot, α is slot pitch angle, β is teeth pitch angle, and $\mathbf{M}_r$ is the remanent magnetization of permanent magnets. The magnetization pattern

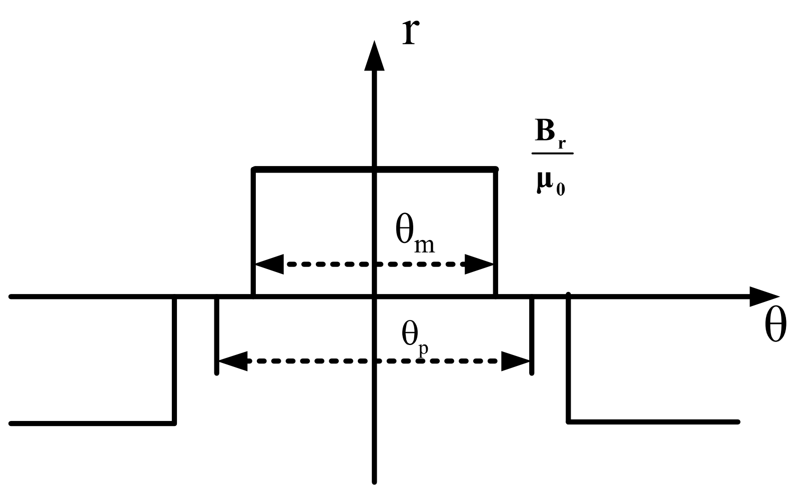

Figure 2.5: Magnetization Distribution

of the alternative placement of north and south magnets in the PM machine produces the magnetic field density with periodicity of π/p . However, the stator slots in machines produce additional spatial harmonics, and in order to include the slot effects accurately, the magnetization pattern shown in the Figure-2.5 is expanded over a period of 2π using Fourier Series and given by

$$\mathbf{M} = \sum_{n=1,2,3,...}^{\infty} M_n \sin\left(n\left(\theta - \delta\right)\right) \tag{2.5}$$

where,

$$M_n = \begin{cases} \frac{4P\mathbf{B_r}}{\mu_o n\pi} \sin\left(\frac{n\pi\theta_m}{\theta_p p}\right) & \text{if } \; \mathrm{n = jp}, \;\; \mathrm{j} = 1, 3, 5.... \\ 0 & \text{otherwise} \end{cases} \tag{2.6}$$

The initial position of i^{th} slots , and j^{th} teeth are given as

$$\begin{aligned} \alpha_i &= \theta_o + \tfrac{2i\pi}{Q} & \forall \, \mathrm{i} \in \{1, Q\} \\ \beta_i &= \theta_o + \alpha + \tfrac{2i\pi}{Q} & \forall \, \mathrm{i} \in \{1, Q\} \end{aligned} \tag{2.7}$$

The magnetization distribution expressed in the equation (2.5) is used to simply the equation (2.1), and variable separable method is used to solve the equations (2.1)-(2.4).

To obtain the complete solution of the governing field equations given in equations (2.1)-(2.4), the knowledge of physical phenomena is required. So, the solution of such problems depends on the boundary conditions and these conditions vary with variations in the machine topologies and magnetic properties of the materials.
Since rotor core is infinitely permeable, all the flux fall normally on the rotor surface.

$$\left.\frac{\partial \mathbf{A_1}}{\partial r}\right|_{r=R_1} = 0 \tag{2.8}$$

The Gauss law provides the continuity of normal flux density at magnet and airgap interface, and hence, we have

$$\mathbf{A_1} = \mathbf{A_2}|_{r=R_2} \tag{2.9}$$

Considering the boundary condition (2.8), which represents the zero tangential component of the flux density at $r = R_1$, and considering the continuity of the radial component of the flux density at $r = R_2$ as represented by equation (2.9), the general solution of the magnetic vector potential [116] in the permanent magnet region can be expressed as

$$\begin{aligned}\mathbf{A_1}(r,\theta) = &\sum_{n=1,2,3....}^{\infty} \left[a_{1n}\tfrac{X_n(r,R_1)}{X_n(R_2,R_1)} + F_n\left(r\right) cos\left(n\delta\right)\right]\cos n\theta \\ + &\sum_{n=1,2,3....}^{\infty} \left[c_{1n}\tfrac{X_n(r,R_1)}{X_n(R_2,R_1)} + F_n\left(r\right)\sin\left(n\delta\right)\right]\sin n\theta\end{aligned} \tag{2.10}$$

where,

$$\begin{aligned}F_n\left(r\right) = &-\tfrac{X_n(r,R_1)}{X_n(R_2,R_1)}\left[\tfrac{R_1}{n}\left(\tfrac{R_1}{R_2}\right)^n f_n^1\left(R_1\right) + f_n\left(R_2\right)\right] \\ &+ \left[\tfrac{R_1}{n}\left(\tfrac{R_1}{r}\right)^n f_n^1\left(R_1\right) + f_n\left(r\right)\right]\end{aligned} \tag{2.11}$$

and

$$f_n\left(r\right) = \begin{cases} \frac{4B_r p}{(1-n^2)\pi} r\cos\left(\frac{n\pi}{2p}\left(1-\alpha_p\right)\right) & \text{if n = jp with j} = 1, 3,... \\ \frac{2B_r}{\pi} r\ln r\cos\left(\frac{\pi}{2}\left(1-\alpha_p\right)\right) & \text{if n = p = 1} \\ 0 & \text{otherwise} \end{cases} \tag{2.12}$$

where, n is number of harmonics, it is worth to mention that the magnetic vector potential given by equation 2.10 contains extra harmonics which in not integral multiple of pole pair number due to the presence of the stator slots. Moreover, X_n, and Y_n are defined as below

$$\begin{aligned}X_n\left(r,R\right) &= \left(\tfrac{r}{R}\right)^n + \left(\tfrac{r}{R}\right)^{-n} \\ Y_n\left(r,R\right) &= \left(\tfrac{r}{R}\right)^n - \left(\tfrac{r}{R}\right)^{-n}\end{aligned} \tag{2.13}$$

Now considering the continuity of tangential component of flux density at both the interfaces $r = R_2$, and $r = R_3$ of the air-gap subdomain, which is mathematically expressed as

$$\frac{1}{\mu_r}\frac{\partial \mathbf{A_1}}{\partial r}\bigg|_{r=R_2} = \frac{\partial \mathbf{A_2}}{\partial r}\bigg|_{r=R_2} \tag{2.14}$$

and,

$$\frac{\partial \mathbf{A_2}}{\partial r}\bigg|_{r=R_3} = \begin{cases} \frac{\partial \mathbf{A_{3i}}}{\partial r}\theta \in [\alpha_i,\alpha_i+\alpha] \\ \frac{1}{\mu_j}\frac{\partial \mathbf{A_{4j}}}{\partial r}\theta \in [\alpha_i+\alpha,\alpha_i+\alpha+\beta] \end{cases} \tag{2.15}$$

the airgap magnetic vector potential can be written as

$$\begin{aligned} \mathbf{A_2}(r,\theta) = & \sum_{n=1,2,3....}^{\infty} \left(a_{2n}\frac{R_2}{n}\frac{X_n(r,R_3)}{Y_n(R_2,R_3)} + b_{2n}\frac{R_3}{n}\frac{X_n(r,R_2)}{Y_n(R_3,R_2)}\right)\cos n\theta \\ + & \sum_{n=1,2,3....}^{\infty} \left(c_{2n}\frac{R_2}{n}\frac{X_n(r,R_3)}{Y_n(R_2,R_3)} + d_{2n}\frac{R_3}{n}\frac{X_n(r,R_2)}{Y_n(R_3,R_2)}\right)\sin n\theta \end{aligned} \tag{2.16}$$

To evaluate the vector potential in region 3i, and region 4j, following boundary conditions are used:

As discussed before, the nonlinear on-load machine simulation shows the least possible relative permeability of teeth is 50. According to the book [79], the flux falls almost normally, if relative permeability of the media is more than 9. Hence, at the lateral edges of the slots and teeth, the radial component of the flux density can be assumed zero, which is mathematically written in equations (2.17) and (2.18). This assumption suggests that the vector potential in both regions are periodic in peripheral direction with periodicity of α and β, respectively.

$$\frac{\partial \mathbf{A_{3i}}}{\partial \theta}\bigg|_{\substack{\theta=\alpha_i \\ \theta=\alpha_i+\alpha}} = 0 \tag{2.17}$$

$$\frac{\partial \mathbf{A_{4j}}}{\partial \theta}\bigg|_{\substack{\theta=\alpha_i+\alpha \\ \theta=\alpha_i+\alpha+\beta}} = 0 \tag{2.18}$$

Moreover, because of infinite permeability of the stator yoke, the tangential components of flux density at $r = R_4$ for slots and yoke interface, and teeth and stator yoke interface are given as below

$$\frac{\partial \mathbf{A_{3i}}}{\partial r}\bigg|_{r=R_4} = 0 \tag{2.19}$$

and,

$$\frac{\partial \mathbf{A_{4j}}}{\partial r}\bigg|_{r=R_4} = 0 \tag{2.20}$$

Considering the boundary conditions expressed by equations (2.17)-(2.20), the vector potentials for slots and teeth subdomain are evaluated as

$$\mathbf{A_{3i}}(r,\theta) = a_{30}^i + \sum_{k=1,2,3....}^{\infty} a_{3k}^i \frac{\alpha R_3}{k\pi}\frac{X_{k\pi/\alpha}(r,R_4)}{Y_{k\pi/\alpha}(R_3,R_4)}\cos\frac{k\pi}{\alpha}(\theta-\alpha_i) \tag{2.21}$$

and,

$$\mathbf{A_{4j}}(r,\theta) = a_{40}^{j} + \sum_{m=1,2,3....}^{\infty} a_{4m}^{j} \frac{\beta R_3}{m\pi} \frac{X m\pi_{/\beta}(r, R_4)}{Y m\pi_{/\beta}(R_3, R_4)} \cos\frac{m\pi}{\beta}(\theta - \beta_i) \tag{2.22}$$

All discussed boundary conditions are used for the calculation of coefficients involved in the magnetic vector potential equations (2.10), (2.16), (2.21) and (2.22). However, the boundary conditions given by the equations(2.8), and (2.17)-(2.20) have been implicitly used in the expression of the vector potential of respective subdomain.

The boundary condition stated in equation (2.9) is applied, and the coefficients a_{1n}, and c_{1n} are determined using a Fourier Series expansion of $\mathbf{A_2}(R_2,\theta)$ over the period of 2π.

$$a_{1n} = \frac{1}{\pi}\int_{0}^{2\pi} \mathbf{A_2}\left(R_2,\theta\right)\cos\left(n\theta\right)d\theta \tag{2.23}$$

and,

$$c_{1n} = \frac{1}{\pi}\int_{0}^{2\pi} \mathbf{A_2}\left(R_2,\theta\right)\sin\left(n\theta\right)d\theta \tag{2.24}$$

Furthermore, to evaluate the coefficients used in equation (2.16) the boundary conditions given by equations (2.14) and (2.15) are used. Expanding $\left.\frac{\partial \mathbf{A_1}(r,\theta)}{\mu_r \partial r}\right|_{r=R_2}$ over a period of 2π, and equating it to $\left.\frac{\partial \mathbf{A_2}(r,\theta)}{\partial r}\right|_{r=R_2}$ gives

$$a_{2n} = \frac{1}{\pi}\int_{0}^{2\pi} \left.\frac{\partial \mathbf{A_1}\left(r,\theta\right)}{\mu_r \partial r}\right|_{r=R_2} \cos\left(n\theta\right)d\theta \tag{2.25}$$

and,

$$c_{2n} = \frac{1}{\pi}\int_{0}^{2\pi} \left.\frac{\partial \mathbf{A_1}\left(r,\theta\right)}{\mu_r \partial r}\right|_{r=R_2} \sin\left(n\theta\right)d\theta \tag{2.26}$$

while, the continuity of the tangential flied intensity at $r = R_3$ represented by equation (2.15) is used to write the Fourier expansion of the tangential field intensity of slot and teeth subdomain over 2π period, and written as

$$b_{2n} = \frac{1}{\pi}\sum_{i=j=1}^{Q}\left(\int_{\alpha_i}^{\alpha_i+\alpha} \left.\frac{\partial \mathbf{A_{3i}}\left(r,\theta\right)}{\partial r}\right|_{r=R_3} \cos\left(n\theta\right)d\theta + \int_{\beta_i}^{\beta_i+\beta} \left.\frac{\partial \mathbf{A_{4j}}\left(r,\theta\right)}{\mu_j \partial r}\right|_{r=R_3} \cos\left(n\theta\right)d\theta\right) \tag{2.27}$$

and,

$$d_{2n} = \frac{1}{\pi}\sum_{i=j=1}^{Q}\left(\int_{\alpha_i}^{\alpha_i+\alpha} \left.\frac{\partial \mathbf{A_{3i}}\left(r,\theta\right)}{\partial r}\right|_{r=R_3} \sin\left(n\theta\right)d\theta + \int_{\beta_i}^{\beta_i+\beta} \left.\frac{\partial \mathbf{A_{4j}}\left(r,\theta\right)}{\mu_j \partial r}\right|_{r=R_3} \sin\left(n\theta\right)d\theta\right) \tag{2.28}$$

For evaluating the coefficients involved in the equations (2.21), and (2.22), the boundary condition of radial flux density continuity at $r = R_3$ (given in the equations (2.29), and (2.30)) are used, that is

$$\mathbf{A_{3i}} = \mathbf{A_2}|_{r=R_3} \forall\theta \in [\alpha_i,\alpha_i + \alpha] \tag{2.29}$$

and,

$$\mathbf{A_{4j}} = \mathbf{A_2}|_{r=R_3} \forall\theta \in [\alpha_i+\alpha,\alpha_i + \alpha + \beta] \tag{2.30}$$

The magnetic vector potential $\mathbf{A_2}|_{r=R_3}$ is expanded over $[\alpha_i, \alpha_i+\alpha]$ for slots, and $[\beta_i, \beta_i+\beta]$ for teeth regions, and equated with $\mathbf{A_{3i}}|_{r=R_3}$, and $\mathbf{A_{4j}}|_{r=R_3}$, which result in following equations

$$a_{30}^{i} = \frac{1}{\alpha} \int_{\alpha_i}^{\alpha_i+\alpha} \mathbf{A_2}(R_3, \theta) d\theta \tag{2.31}$$

$$a_{3k}^{i} = \frac{2}{\alpha} \int_{\alpha_i}^{\alpha_i+\alpha} \mathbf{A_2}(R_3, \theta) \cos \frac{k\pi}{\alpha} (\theta - \alpha_i)\, d\theta \tag{2.32}$$

$$a_{40}^{j} = \frac{1}{\beta} \int_{\beta_i}^{\beta_i+\beta} \mathbf{A_2}(R_3, \theta) d\theta \tag{2.33}$$

and,

$$a_{4m}^{j} = \frac{2}{\beta} \int_{\alpha_i}^{\alpha_i+\alpha} \mathbf{A_2}(R_3, \theta) \cos \frac{m\pi}{\beta} (\theta - \beta_i)\, d\theta \tag{2.34}$$

The coefficients governing integral equations (2.23)-(2.34) are further simplified into simultaneous linear equations and are briefed in Appendix B.

2.3.2 No load Magnetic Field Calculation

The definition of vector potential is used to get the following equations,

$$\mathbf{B_r} = \frac{1}{r}\frac{\partial \mathbf{A}}{\partial \theta} \tag{2.35}$$

$$\mathbf{B_\theta} = -\frac{\partial \mathbf{A}}{\partial r} \tag{2.36}$$

and the radial and tangential component of flux density in all regions are given by,

In the region 1

$$\begin{aligned} \mathbf{B_{1r}}(r, \theta) = &- \sum_{n=1,2,3....}^{\infty} \tfrac{n}{r}\left(a_{1n}\tfrac{X_n(r,R_1)}{X_n(R_2,R_1)} + F_n\left(r\right) sin\left(n\phi\right)\right) \sin n\theta \\ &+ \sum_{n=1,2,3....}^{\infty} \tfrac{n}{r}\left(c_{1n}\tfrac{X_n(r,R_1)}{X_n(R_2,R_1)} + F_n\left(r\right) \cos\left(n\phi\right)\right) \cos n\theta \end{aligned} \tag{2.37}$$

and,

$$\begin{aligned}\mathbf{B_{1\theta}}(r,\theta) = &-\sum_{n=1,2,3....}^{\infty}\left(a_{1n}\tfrac{n}{r}\tfrac{Y_n(r,R_1)}{X_n(R_2,R_1)} + F_n'(r)\,sin\,(n\phi)\right)\cos n\theta \\ &-\sum_{n=1,2,3....}^{\infty}\left(c_{1n}\tfrac{n}{r}\tfrac{Y_n(r,R_1)}{X_n(R_2,R_1)} + F_n'(r)\cos(n\phi)\right)\sin n\theta\end{aligned} \tag{2.38}$$

In the region 2

$$\begin{aligned}\mathbf{B_{2r}}(r,\theta) = &-\sum_{n=1,2,3....}^{\infty}\left(a_{2n}\tfrac{R_2}{r}\tfrac{X_n(r,R_3)}{Y_n(R_2,R_3)} + b_{2n}\tfrac{R_3}{r}\tfrac{X_n(r,R_2)}{Y_n(R_3,R_2)}\right)\sin n\theta \\ &+\sum_{n=1,2,3....}^{\infty}\left(c_{2n}\tfrac{R_2}{r}\tfrac{X_n(r,R_3)}{Y_n(R_2,R_3)} + d_{2n}\tfrac{R_3}{r}\tfrac{X_n(r,R_2)}{Y_n(R_3,R_2)}\right)\cos n\theta\end{aligned} \tag{2.39}$$

and,

$$\begin{aligned}\mathbf{B_{2\theta}}(r,\theta) = &-\sum_{n=1,2,3....}^{\infty}\left(a_{2n}\tfrac{R_2}{r}\tfrac{Y_n(r,R_3)}{Y_n(R_2,R_3)} + b_{2n}\tfrac{R_3}{r}\tfrac{Y_n(r,R_2)}{Y_n(R_3,R_2)}\right)\cos n\theta \\ &-\sum_{n=1,2,3....}^{\infty}\left(c_{2n}\tfrac{R_2}{r}\tfrac{Y_n(r,R_3)}{Y_n(R_2,R_3)} + d_{2n}\tfrac{R_3}{r}\tfrac{Y_n(r,R_2)}{Y_n(R_3,R_2)}\right)\sin n\theta\end{aligned} \tag{2.40}$$

In the region 3i

$$\mathbf{B_{3i,r}}(r,\theta) = -\sum_{k=1,2,3....}^{\infty} a_{3k}^{i}\frac{R_3}{r}\frac{X_{k\pi/\alpha}(r,R_4)}{Y_{k\pi/\alpha}(R_3,R_4)}\sin\frac{k\pi}{\alpha}(\theta-\alpha_i) \tag{2.41}$$

and,

$$\mathbf{B_{3i,\theta}}(r,\theta) = -\sum_{k=1,2,3....}^{\infty} a_{3k}^{i}\frac{R_3}{r}\frac{Y_{k\pi/\alpha}(r,R_4)}{Y_{k\pi/\alpha}(R_3,R_4)}\cos\frac{k\pi}{\alpha}(\theta-\alpha_i) \tag{2.42}$$

In the region 4j

$$\mathbf{B_{4j,r}}(r,\theta) = -\sum_{m=1,2,3....}^{\infty} a_{4m}^{j}\frac{R_3}{r}\frac{X_{m\pi/\beta}(r,R_4)}{Y_{m\pi/\beta}(R_3,R_4)}\sin\frac{m\pi}{\beta}(\theta-\beta_i) \tag{2.43}$$

and,

$$\mathbf{B_{4j,\theta}}(r,\theta) = -\sum_{m=1,2,3....}^{\infty} a_{4m}^{j}\frac{R_3}{r}\frac{Y_{m\pi/\beta}(r,R_4)}{Y_{m\pi/\beta}(R_3,R_4)}\cos\frac{m\pi}{\beta}(\theta-\beta_i) \tag{2.44}$$

2.3.3 Cogging Torque, Flux Linkage, and Phase Voltage Calculations

The cogging torque is obtained using the Maxwell Stress Tensor [69], the integration is taken around the permanent magnet surface and is given by

$$T = \frac{LR_2^2}{\mu_o}\int_0^{2\pi}\mathbf{B_{2r}}(R_2,\theta)\mathbf{B_{2\theta}}(R_2,\theta)\,d\theta \tag{2.45}$$

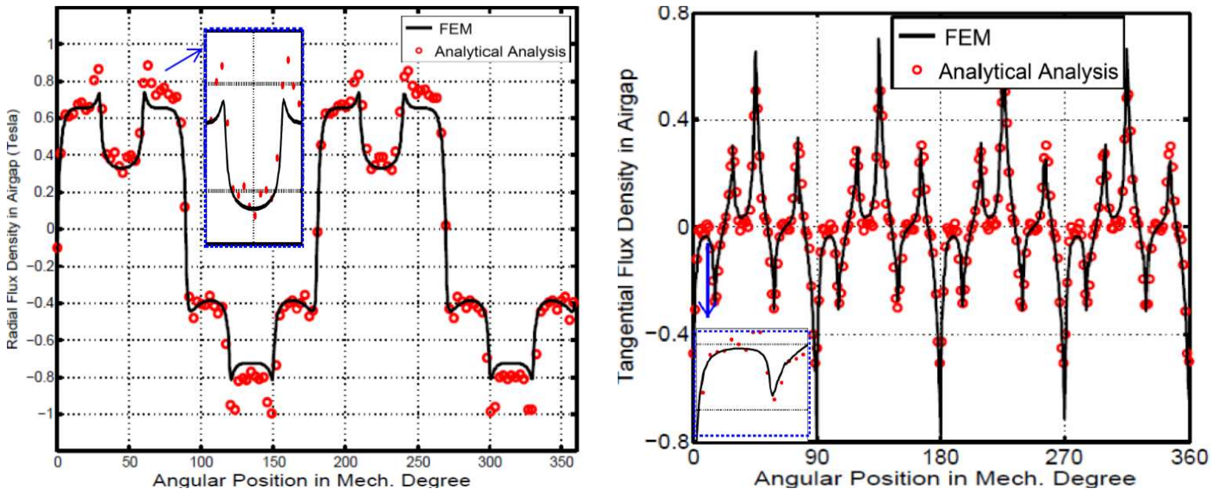

(a) Radial Component

(b) Tangential Component

Figure 2.6: Airgap Flux Density Corresponding to $\mu_j = 10$

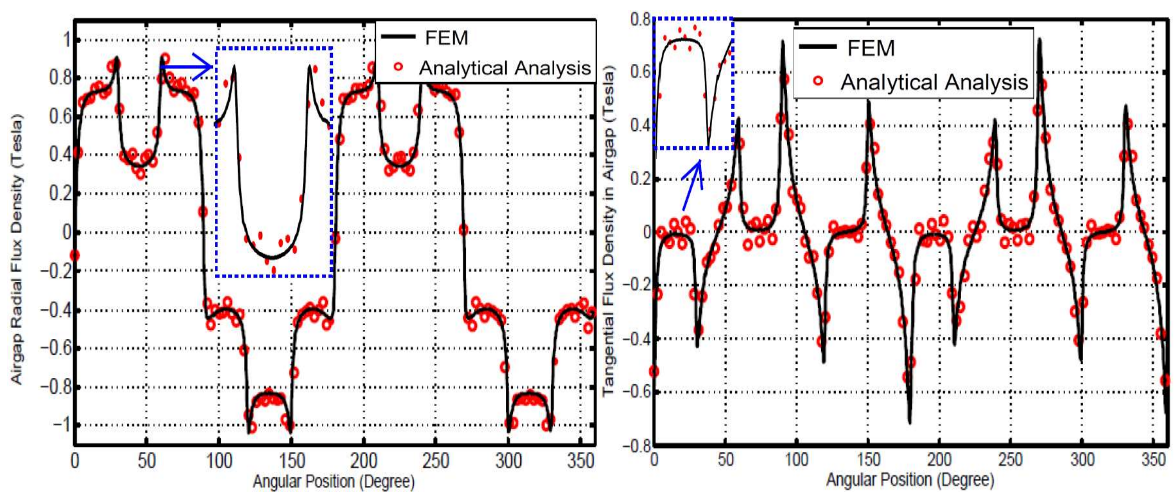

(a) Radial Component

(b) Tangential Component

Figure 2.7: Airgap Flux Density Corresponding to $\mu_j = 50$

For the phase flux linkage calculation, the coil is approximated as a current sheet at the slot opening. The flux linkage is predicted by the integral of the radial flux density distribution along the stator bore [121]:

$$\psi_l = 2LR_3N\sum_n \frac{K_pK_{so}}{n}\left(\mathbf{B_{2rs}}\left(R_{3,}\theta\right)K_{dsm} + \mathbf{B_{2rc}}\left(R_{3,}\theta\right)K_{dcm}\right) \tag{2.46}$$

where, l represents phase: A, B, & C and N is the number of turns per phase, $B_{2rs}\left(R_{3,}\theta\right)$ and $B_{2rc}\left(R_{3,}\theta\right)$ are the sine and cosine harmonics of the radial flux density at stator bore, K_p is the pitch factor, K_{so} is the slot opening factor, K_{dsl} and K_{dcl} are the distribution factors of phase m for the sine and cosine flux density harmonics, respectively. These

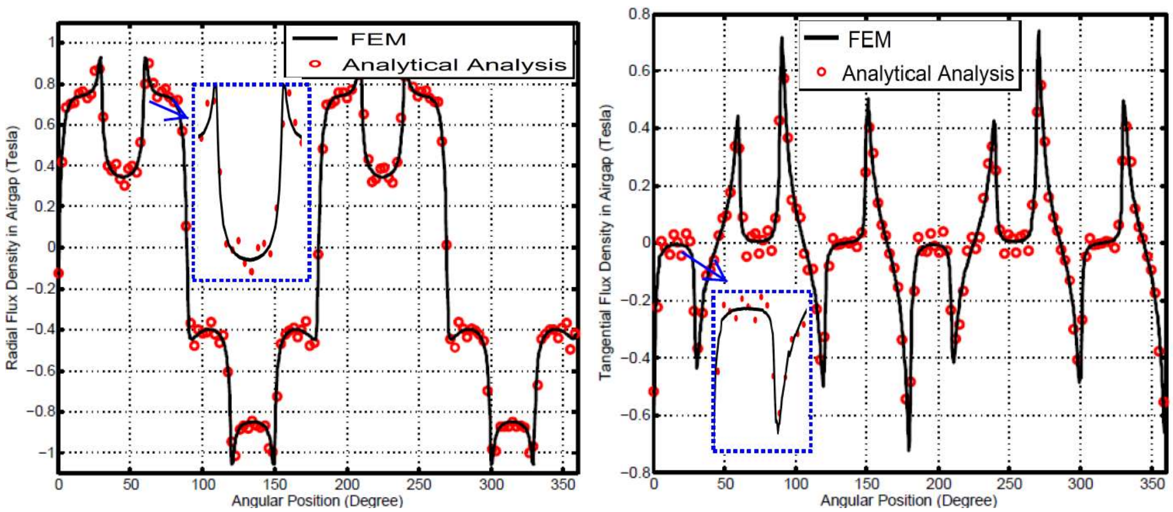

(a) Radial Component (b) Tangential Component

Figure 2.8: Airgap Flux Density Corresponding to $\mu_j = 100$

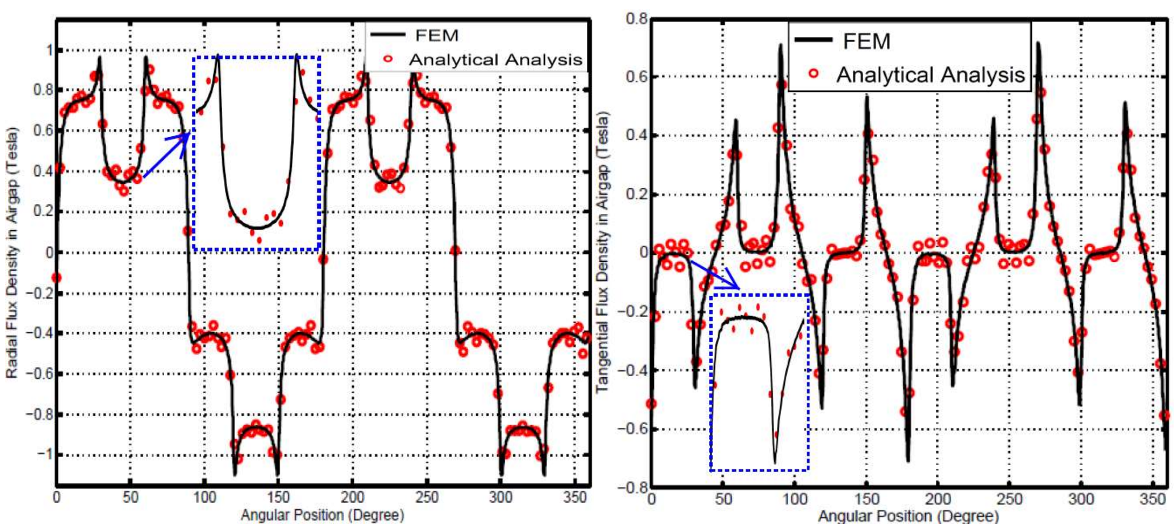

(a) Radial Component (b) Tangential Component

Figure 2.9: Comparison of Airgap Flux Density Corresponding to $\mu_j = 500$

factors are given by

$$\mathbf{B_{2rs}}(R_3, \theta) = -\left(a_{2n}\frac{R_2}{R_3}\frac{2}{Y_n(R_2, R_3)} + b_{2n}\frac{X_n(R_3, R_2)}{Y_n(R_3, R_2)}\right)\sin n\theta \tag{2.47}$$

$$\mathbf{B_{2rc}}(R_3, \theta) = \left(c_{2n}\frac{R_2}{R_3}\frac{2}{Y_n(R_2, R_3)} + d_{2n}\frac{X_n(R_3, R_2)}{Y_n(R_3, R_2)}\right)\cos n\theta \tag{2.48}$$

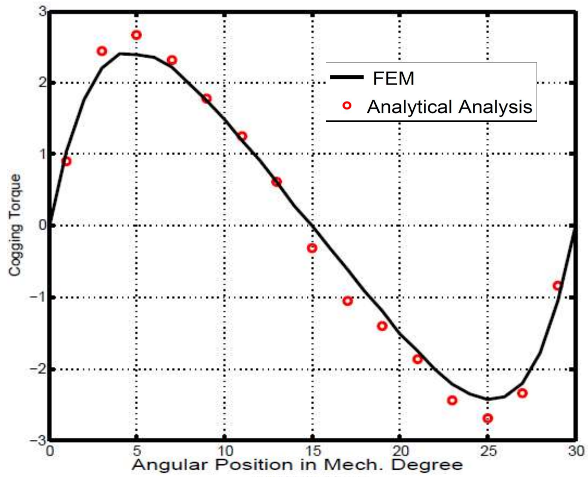

(a) Corresponding to $\mu_j = 10$

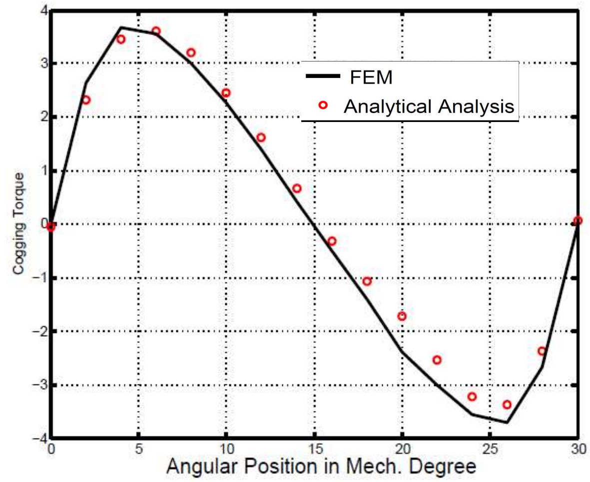

(b) Corresponding to $\mu_j = 50$

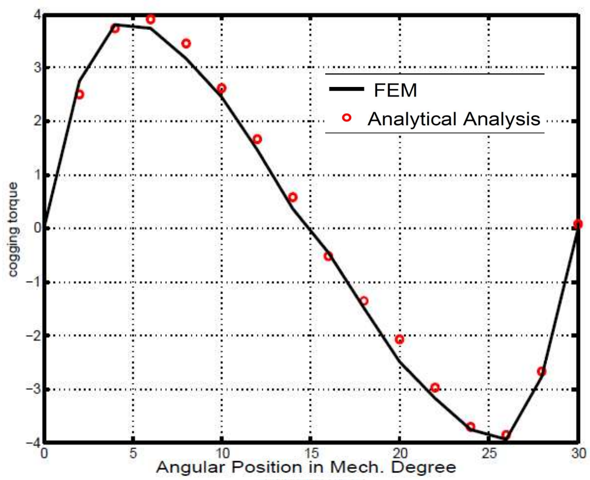

(c) Corresponding to $\mu_j = 100$

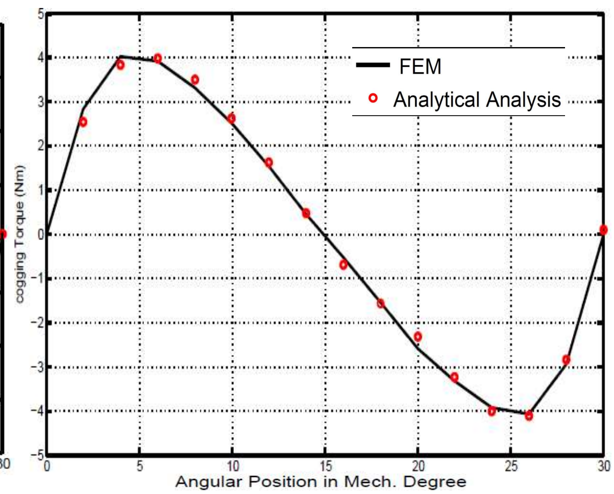

(d) Corresponding to $\mu_j = 500$

Figure 2.10: Comparison of Cogging Torque

$$K_p = \sin \frac{n\theta_c}{2} \tag{2.49}$$

$$K_{so} = \frac{\sin\left({}^{n\theta_o}/_2\right)}{{}^{n\theta_o}/_2} \tag{2.50}$$

$$K_{dsl} = \frac{1}{N_c} \sum_{s=1}^{N_c} C_{ds} \sin\left(n\theta_{cs}\right) \tag{2.51}$$

$$K_{dcl} = \frac{1}{N_c} \sum_{s=1}^{N_c} C_{ds} \cos\left(n\theta_{cs}\right) \tag{2.52}$$

where, N_c is number of coils per phase, θ_c is the coil pitch i.e., coil span, θ_{cs} is the position of the s^{th} coil of the phase l, C_{ds} determine the direction of winding : 1 or -1 for positive or negative direction of the s^{th} coil of the phase l, respectively.

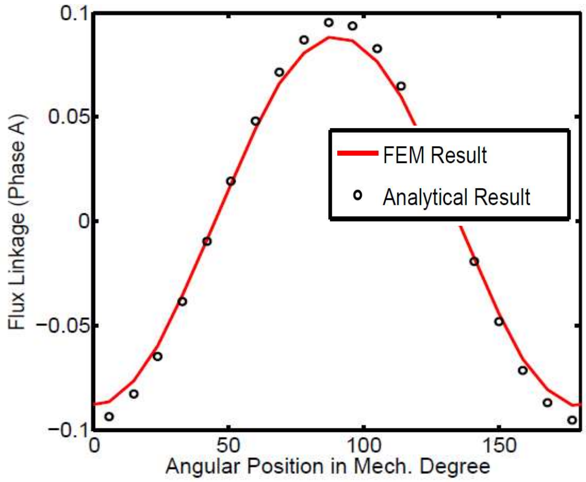

(a) Corresponding to $\mu_j = 10$

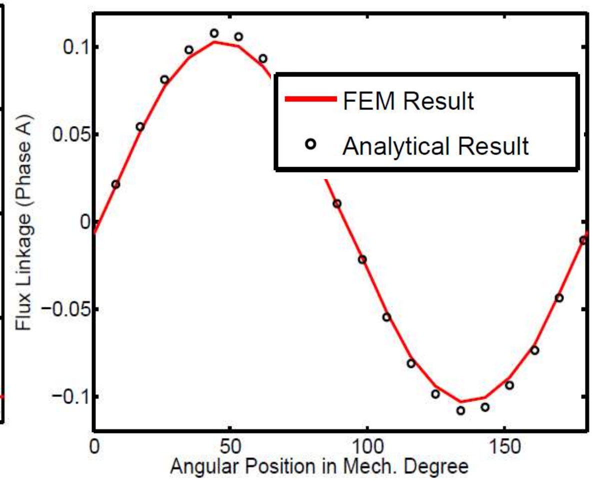

(b) Corresponding to $\mu_j = 50$

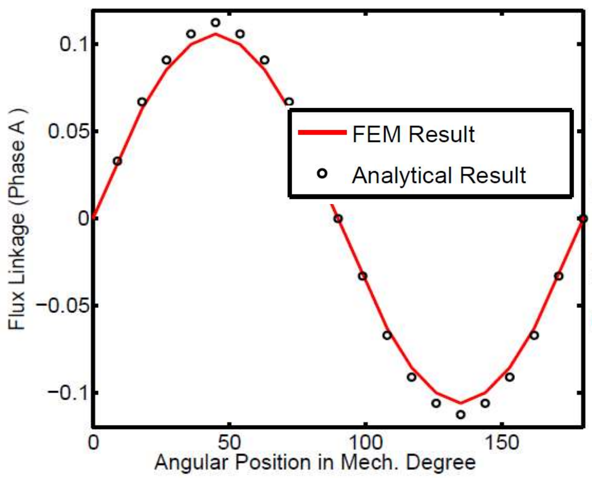

(c) Corresponding to $\mu_j = 100$

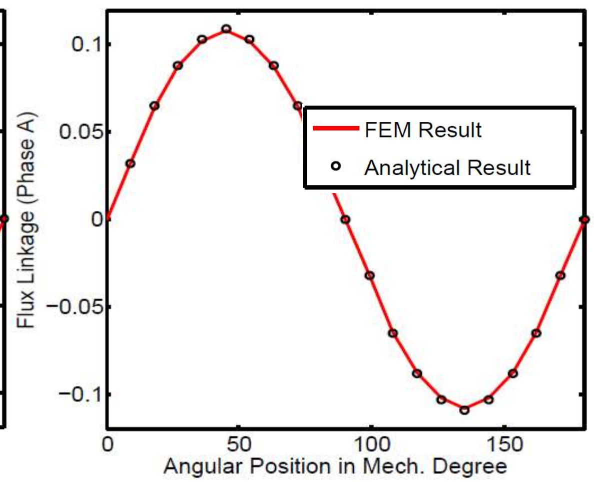

(d) Corresponding to $\mu_j = 500$

Figure 2.11: Comparison of Flux Linkage

Equation (2.46) is used for the phase voltage calculation and given as

$$E_l = \omega_r \frac{d\psi_l}{d\theta} \tag{2.53}$$

2.4 Finite Element Analysis and Results Verification

For the validation of proposed analytical model, FEM is used as numerical technique. The machine, whose dimensional details are given in the Table 2.1, is simulated in ANSYS MAXWELL 18.0 software as shown in Figure-F.1. For the simulation model, two dimensional analysis is used and the developed model is enclosed in the region. The boolean boundary condition is imposed on the region. In FEM modeling, the stator yoke

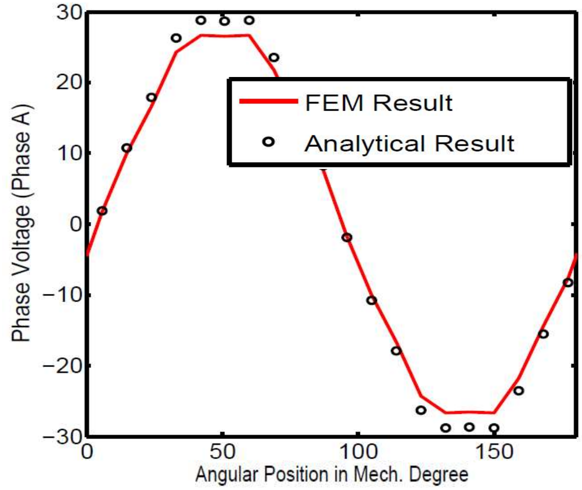

(a) Corresponding to $\mu_j = 10$

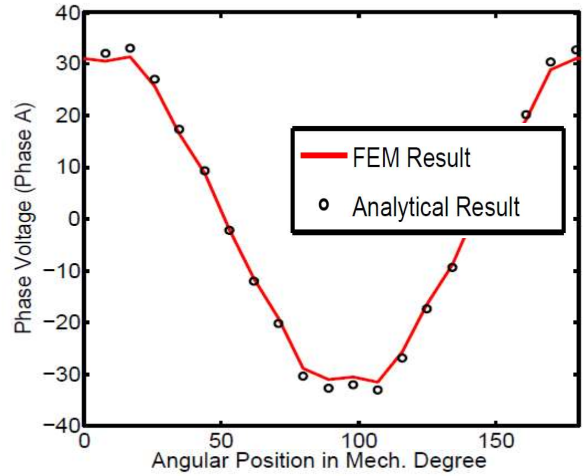

(b) Corresponding to $\mu_j = 50$

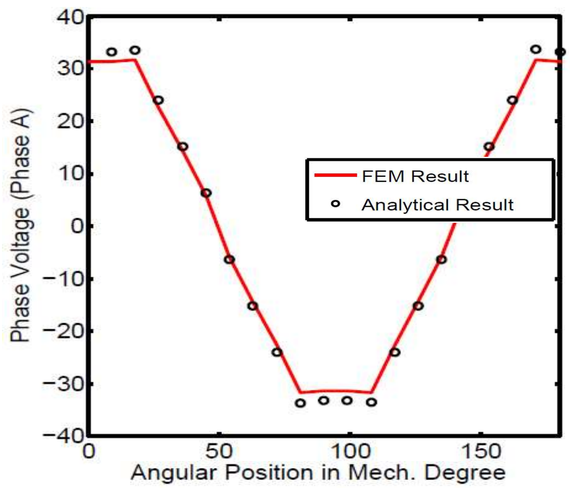

(c) Corresponding to $\mu_j = 100$

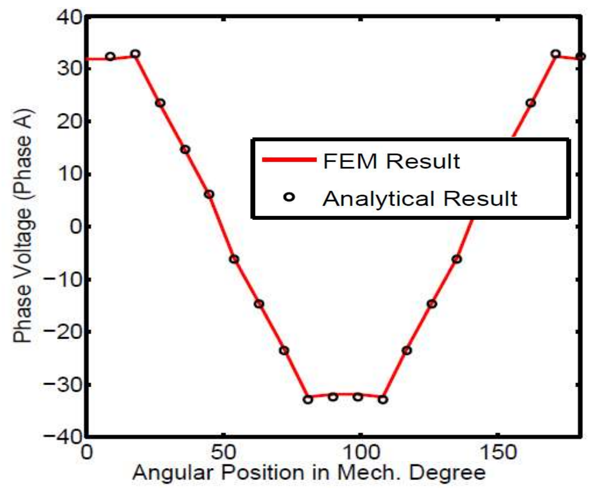

(d) Corresponding to $\mu_j = 500$

Figure 2.12: Comparison of Phase Voltage

and rotor core are assigned for iron having 4000 relative permeability, while tooth of the stator is simulated for four different relative permeability i.e., four different FEM model with μ_j=10, 50, 100, and 500. Firstly, both radial and tangential components of air gap flux density are evaluated for comparison. For analytical analysis, the harmonics in magnets and airgap regions N_{max}, slot region K_{max} and teeth region M_{max} are taken 40, 30 and 30 respectively. Figures (2.6), (2.7), (2.8) and (2.9) compare the analytical and FEM results for the radial and tangential components of the airgap magnetic field. The comparative study of analytical and FEM show the results agreement and hence, validate the analytical model. However, in Figure (2.6) discrepancy in results is observed. This happens due to the assumption that the lateral edges of the slot are highly permeable.

To further investigate the influence of the magnetic saturation on the machine no-load performance parameters, cogging torque, flux linkage, and phase voltage are studied using both analytical and FEM methods. For the analysis of flux linkage and phase voltage, the number of phase coils is taken 50 and machine is rotated with 1500 rpm. In Figure (2.10), calculated cogging torques are compared, and the analysis shows a reduction of cogging torque with lower relative permeability of the teeth. The Figures (2.11) and (2.12) depict comparison of analytical and FEM results for flux linkage and phase voltage respectively. The study of linkage flux, and phase voltage also show the reduction with lower teeth permeability.

2.5 Conclusion

In this chapter, an analytical model of study for saturated PM machine is developed. The results obtained from analytical analysis are compared with the simulation model. The close agreement of both results ensures the accuracy of the developed model. However, at low relative permeability of the teeth, high discrepancy in the results are obtained. Moreover, the reduction of airgap flux density, and machine performance parameters with the lower teeth permeability is found. It is due to the high airgap reluctance in case of saturation. However, in practical machine, the magnetic saturation level would be different for different teeth, hence the effective discrepancy in the practical case would be relatively less.